J. Fluid Mech. (1987), *vol.* 184, *pp.* 423–444
Printed in Great Britain

A description of the organized motion in the turbulent far wake of a cylinder at low Reynolds number

By **R. A. ANTONIA, L. W. B. BROWNE, D. K. BISSET**
Department of Mechanical Engineering, University of Newcastle, N.S.W., 2308, Australia

AND **L. FULACHIER**
Institut de Mécanique Statistique de la Turbulence, Université d'Aix-Marseille,
13003 Marseille, France

(Received 20 August 1986 and in revised form 13 March 1987)

The topology of the organized motion has been obtained in the slightly heated self-preserving far wake of a circular cylinder at a Reynolds number, based on the cylinder diameter, of about 1200. In a frame of reference moving with the organized motion, the toplogy in the plane of main shear reduces to a succession of centres and saddles, located at about the wake half-width. Centres are identifiable by large values of spanwise vorticity associated with the coherent large-scale motion. Saddles occur at the intersection of converging and diverging separatrices, the latter being identifiable with the high strain rate due to the large-scale motion. Large values of the longitudinal turbulence intensity associated with the smaller-scale motion occur at the centres. High values of the normal and shear stresses, the temperature variance and heat fluxes associated with the large-scale motion occur on either side of each saddle point along the direction of the diverging separatrix. Contours for the production of energy and temperature variance associated with the small-scale motion are aligned along the diverging separatrices, and have maxima near the saddle point. Contours for one component of the dissipation of small-scale temperature variance also have a high concentration along the diverging separatrix. Flow visualizations in the far wake suggest the existence of groups of three-dimensional bulges which are made up of clusters of vortex loops.

1. Introduction

Coherent structures in the turbulent near-wake of a circular cylinder have been studied (e.g. Cantwell & Coles 1983; Hayakawa & Hussain 1985; Kiya & Matsumura 1985) using conditional sampling and averaging techniques. The emphasis in all these studies has been on the topology of the structures: in a frame of reference moving with the structures, conditionally averaged velocity vectors in the plane of main shear show a pattern of critical points such as centres and saddles. Generally, this approach, which is based on the assumption of similarity in time (Cantwell 1979), provides a framework for a unified description of coherent structures in different turbulent shear flows or in different regions of the same turbulent shear flow.

The existence of coherent structures in the far wake (typically for distances greater than about 100*d*, where *d* is the cylinder diameter) has been established by flow visualization (e.g. Taneda 1959; Keffer 1965; Papailiou & Lykoudis 1974; Cimbala

1984, 1985) or by hot-wire measurements (e.g. Grant 1958; Keffer 1965; Townsend 1979; Mumford 1983). Although there is a general consensus that these structures are part of a secondary vortex street, distinguishable from the near-wake Kármán vortex street, there is a lack of agreement on the mechanism responsible for the formation of the far-wake coherent structures. Whereas the flow visualization of Papailiou & Lykoudis (1974) suggested a possible residual influence of the Kármán street in the far wake, Budny, Kawall & Keffer (1979) found no measurable frequency-centred activity attributable to the Kármán street beyond about 65 cylinder diameters. Matsui & Okude (1981, 1983) proposed that the far-wake structures are formed as a result of the amalgamation of the near-wake Kármán vortices. The flow visualization of Wlezien (1981) suggested that the far-wake structures are a result of local instabilities in the mean shear and are not directly related to the near wake. Cimbala (1984, 1985) also indicated that the far-wake structures result from a hydrodynamic instability of the mean wake profile, quite independently of the near-wake vortices. Wygnanski, Champagne & Marasli (1986) have shown that vorticity contours obtained for the far wake using linear stability theory are not inconsistent with experimental observations. It has been shown that far-wake-type structures occur in flows with no near-wake Kármán vortices (see, for example, Cimbala 1984, 1985; Ferre i Vidal 1986). However, Bevilaqua & Lykoudis (1978) and Wygnanski *et al.* (1986) suggest that the behaviour of self-preserving wakes depends on the initial conditions, for example, the presence or lack of periodicity in the near wake. Ferre i Vidal noted that although the self-preserving region of the wake is dominated more by entrainment and engulfment than by initial conditions, the latter can still exert some influence on the downstream development of the flow.

Lumley (1981) noted that important differences have been found between structures in the initial and fully developed regions of various turbulent shear flows. Regardless of the precise manner in which the far-wake structures originate, the available evidence suggests that there may be differences between these structures and those in the near wake. It is generally assumed (the evidence is not conclusive) that the near-wake structures are essentially two-dimensional, while the three-dimensionality of the far-wake structures has been discussed by Barsoum, Kawall & Keffer (1978) and Cimbala (1984). Flow visualizations (e.g. Taneda 1959; Keffer 1965; Cimbala 1984, 1985) indicate that the far-wake structures occur irregularly in space and time, with a tendency to appear in groups, in contrast to the more deterministic, if not periodic, appearance of the near wake. Our photograph, figure 1, shows both the near wake and part of the far wake of a cylinder. The wake is made visible by injecting white dye (rhodorsil) near the rear stagnation point of the cylinder. The Reynolds number ($R_d = 480$, where $R_d = U_1 d/\nu$, U_1 is the free-stream velocity and ν is the kinematic viscosity of the fluid) is sufficiently large for the wake to be 'turbulent' (e.g. Cimbala 1985 considers the wake to be turbulent if $R_d \gtrsim 160$). The Kármán street, visible in the near wake, tends to become disorganized relatively quickly (it disappears at about $40d$) but some organization reappears further downstream in the form of bulges, identified by strong dye concentrations. The bulges often appear in groups and are often antisymmetrical about the centreline.

The main aim of the present study is to provide a detailed topological description of the far-wake coherent structures, in the plane of main shear. The focus is on the groups of antisymmetrical structures that have been identified in flow visualizations and in other studies (e.g. Townsend 1979; Mumford 1983; Browne, Antonia & Bisset 1986) in the far wake. The wake-generating cylinder was heated so that temperature could be used, as in the plane-jet study of Antonia *et al.* (1986), for detecting coherent

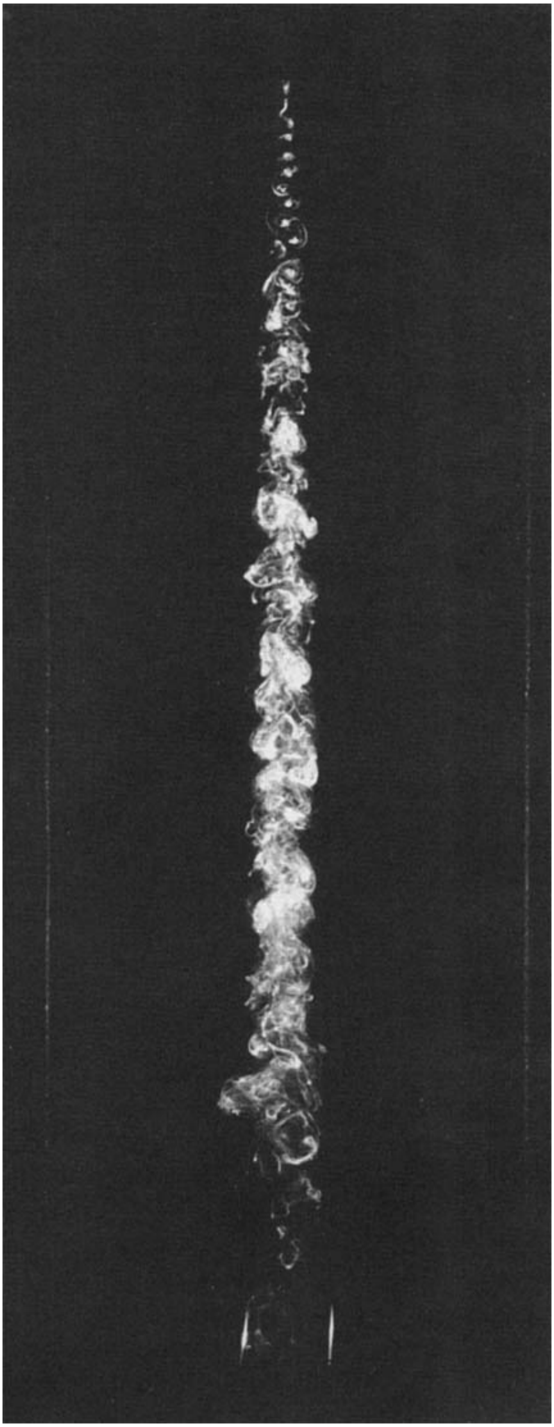

FIGURE 1. Photograph, in the (x, y)-plane, of a wake in the range $0 \leqslant x/d \lesssim 180$. $R_d = 430$.

structures. The introduction of temperature in the flow also allows a comparison to be made between velocity and temperature fields, this being the second aim of this study. This comparison is quantified in the context of contributions that the selected structures make to the average transfers of momentum and heat. A third aim of this study is to provide some insight into the physical nature of the structures by relating wind-tunnel measurements to the patterns obtained by flow-visualization techniques in a water tunnel.

2. Experimental details

The wind tunnel used was a non-return blower-type facility with a working section 350 × 350 mm, 2.4 m long. Measurements were made with zero pressure gradient at a distance of 420 diameters downstream of a circular cylinder ($d = 2.67$ mm, aspect ratio = 131) and a Reynolds number $R_d \approx 1200$ (the free-stream velocity U_1 was nominally 6.7 m/s). The cylinder was heated (100 W) so that temperature was a passive marker of the self-preserving region of the flow. Full details of the tunnel are given in Browne & Antonia (1986), while the two experimental arrangements that were used are described in detail in Browne *et al.* (1986) and only a brief description is given here.

In the first arrangement, four cold wires with a Δz^* span of 1.8 and an X-probe/cold-wire assembly, located at the centre of this span, formed an integral part of the same rake (a total of seven wires) which was traversed across the wake from $y^* = -2$ to $y^* = +1.6$. Here, the asterisk denotes normalization by the half-width $L = 12.3$ mm; when it appears in association with a velocity or a temperature it will denote normalization by a velocity scale $U_0 = 0.36$ m/s, the mean velocity defect on the wake centreline, and a temperature scale $T_0 = 0.82$ K, the mean temperature excess on the centreline relative to the free-stream temperature T_1. The fixed rake used in the second arrangement consisted of four cold wires spanning a distance $\Delta z^* = 0.82$ at $y^* = -1.22$. The X-probe/cold-wire combination, located centrally in the z-direction with respect to the four cold wires, was moved from $y^* = -0.77$ to $y^* = +1.22$. The signals from the fixed rake of cold wires in this second arrangement were used for detection and, by comparing with the detections obtained from the single movable cold wire in that arrangement, the y^* variation of the temperature-front positions could be obtained. Data from the first arrangement were used for the y^* positions not covered by the second arrangement.

All cold wires were made of 0.63 μm diameter Pt–10% Rh Wollaston and had an active length of 1 mm. They were operated with in-house constant current (= 0.1 mA) circuits. The hot wires of the X-probe were made of 5 μm diameter Pt–10% Rh with an active length of 0.85 mm, separated by 0.8 mm. The cold wire associated with the X-probe was placed 0.5 mm in front of the centre of the X-probe and perpendicular to the plane of the probe. The hot wires were operated with constant-temperature circuits at an overheat of 1.8. Velocity, yaw and temperature calibrations were carried out using an HP computer and data acquisition system with a sampling frequency of 10 Hz. This computer was also used to monitor the performance of all wires during the experiments. The fluctuating voltages from all wires were low-pass filtered at 1 kHz and sampled at 2 kHz per channel into a PDP 11/34 computer using an 11 bit plus sign sample and hold A/D unit. Subsequent processing of the data was made on either the 11/34 or a VAX 11/780.

As a result of heating the cylinder, it may be argued that fluid elements heated by the cylinder are affected by buoyancy over the total time required for them to be convected to the far wake. However, at $x/d = 420$, the ratio Gr/R_d^2, where Gr is the Grashof number, defined by $Gr = gL^3T_0/\nu^2T_1$, is 9×10^{-6}. If the lengthscale x, the distance from the source of heating, is used instead of L, the value of Gr/R_d^2 is 8×10^{-4}, quite small enough to support the claim that temperature acts as a passive marker of the far wake. Also, measured mean velocity and mean temperature profiles over a distance $200 \lesssim x/d \lesssim 700$ showed good symmetry about virtually the same centreline. Further, as noted in Browne & Antonia (1986), conventional statistics of the longitudinal velocity fluctuation u, the lateral velocity fluctuation v and the product uv obtained with an X-wire at $x/d = 420$ were the same, irrespective of whether the cylinder was heated or not.

The Institut de Mécanique Statistique de la Turbulence's water tunnel at the Université d'Aix-Marseille was used for the flow visualizations and has been described in detail by Dumas, Bonmarin & Fulachier (1982). The cylinder ($d = 3$ mm) was inserted centrally across the flow 30 cm downstream of the beginning of the 20 × 20 cm working section. The cylinder was hollow to enable the injection of dye close to the rear stagnation point midway between the working-section walls. Dye could also be injected in the tunnel contraction upstream of the working section via two small tubes (0.2 mm diameter) at $x/d = 180$. Photographs in the (x, y)-planes were taken with the use of flash lighting and by illuminating a narrow (0.5 cm wide) section of the flow. Reynolds numbers of 280 and 430 were used, corresponding to values of U_1 of 9.3 and 14.3 cm/s respectively. These Reynolds numbers are larger than the value of about 160 at which the wake is considered to be 'turbulent' (e.g. Cimbala 1985).

3. Conditional averages

3.1. *Definitions*

A quantitative discussion of coherent structures requires the introduction of a conditional average, defined in §3.2, which can be obtained once the structures are identified. Denoting this average by angular brackets, any instantaneous variable $F(\equiv U, V \text{ or } T)$ can be expressed by the double decomposition (e.g. Hussain 1983)

$$F = \langle F\rangle + F_s. \tag{1}$$

The component F_s has been described in previous studies as that part of F associated with the random, or sometimes, incoherent motion. Neither random nor incoherent seems appropriate, especially in view of the relatively organized spatial distributions of $\langle F_s^2\rangle$ (e.g. Cantwell & Coles 1983). With $\langle F\rangle$ identifiable with the large-scale motion, it seems reasonable to associate F_s with the remaining smaller-scale motion, noting that the values obtained for F_s are determined as much by the smaller-scale motion's phase relationship with the large-scale motion as by its magnitude.

An alternative approach is to interpret F, using a triple decomposition (e.g. Hussain 1983), as the sum of a global mean $\overline{F}$ (the overbar denotes an average over time), a perturbation $\tilde{F}$ due to the large-scale motion, and the small-scale contribution F_s:

$$F = \overline{F} + \tilde{F} + F_s. \tag{2}$$

When conditional averaging is applied to (2), the result, on the assumption that the small-scale and large-scale motions are uncorrelated is

$$\langle F\rangle = \overline{F} + \tilde{F}. \tag{3}$$

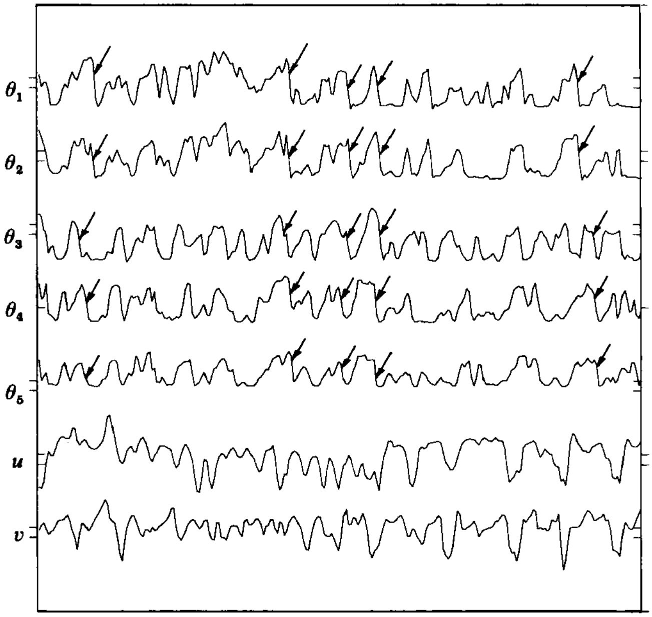

FIGURE 2. Simultaneous temperature and velocity signals obtained with a rake of wires aligned in the spanwise direction at $y^* = -1.42$. The five upper traces are temperature signals (θ_1–θ_5) while the two lower traces are velocity signals u and v obtained with an X-probe immediately downstream of the cold wire which provides signal θ_3. The vertical scale is arbitrary. The traces are shown for a duration of 0.127 s. Temperature fronts are identified by arrows.

The perturbation $\tilde{F}$ is thus seen as the difference between the conditional average of F and its global mean.

The double decomposition (1) tends to give greater emphasis to the large-scale motion than the triple decomposition (2), in which $\tilde{F}$ is superposed on a global or mean motion. Cantwell & Coles (1983) used both double and triple decompositions but noted that the double decomposition was more appropriate for studying the coherent motion in the near wake. Hayakawa & Hussain (1985) used a double decomposition to present measurements in the range $10d$–$40d$ downstream of a circular cylinder. Kiya & Matsumura (1985) used a triple decomposition to present measurements at a distance $8d$ from the cylinder. In the present work, we make use of both (1) and (2): whereas (1) focuses on the coherent motion more appropriately than (2), the use of (2) permits an assessment to be made of the relative contributions to the Reynolds stresses and heat fluxes from the large-scale and small-scale motions. It is in this sense that the triple decomposition was used by Antonia *et al.* (1986) and Browne *et al.* (1986). Using the conventional Reynolds decomposition

$$F = \overline{F} + F', \tag{4}$$

where F' is the conventional turbulent fluctuation. Using (2), F' may be written as

$$F' = \tilde{F} + F_s,$$

i.e. F' can be thought of as the sum of the perturbation due to the large-scale motion and a small-scale contribution. The Reynolds-averaged stresses and heat fluxes can be expressed as

$$\overline{F'G'} = \overline{\tilde{F}\tilde{G}} + \overline{F_s G_s}, \tag{5}$$

where F and G represent either U, V or T.

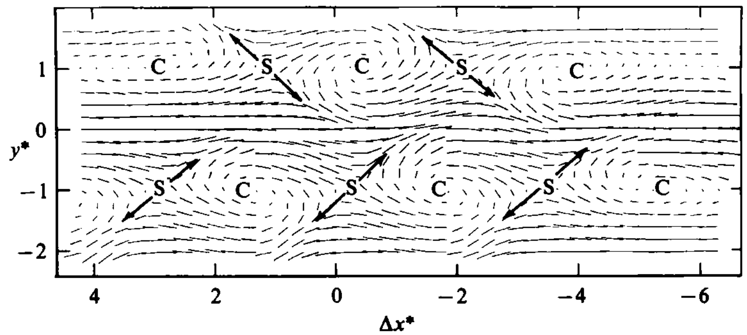

FIGURE 3. Velocity vectors relative to an observer moving right to left with a convection velocity $U_c = 0.97U_1$. In this and subsequent figures, C and S denote centres and saddles respectively, while arrows identify diverging separatrices.

3.2. *Formation of conditional averages*

Since all averages were formed on the computer from digital time series, it is appropriate to define our conditional average $\langle F \rangle$ within this context. The time series representing F comprises N equally spaced values F_j $(j = 1, \ldots, N)$. If j_i $(i = 1, 2, \ldots, n)$ are values of j at which detections occur, then the conditional average of F corresponding to a total number n of detections is given by

$$\langle F \rangle_k = \frac{1}{n} \sum_{i=1}^{n} F_{j_i+k}, \tag{6}$$

where k is the distance from j_i, expressed as a number of data points.

The detection scheme which yields the values of j_i, (6), has been described in Browne *et al.* (1986). Briefly, it consists of an algorithm for identifying temperature fronts in the rake temperature signals, such as shown in figure 2. The fronts are characterized by a relatively sharp decrease in temperature occurring almost simultaneously on all the rake signals. A modified VITA detection process was used in which the VITA criteria, relating to the variance and sign change of data in a movable window, were applied to a signal obtained by averaging the cold-wire signals. Also a shape check was used to ensure, for the averaged signal, that the data leading up to the change and the data after the change should not have a rapidly changing mean. The probability density function of the time difference Δt between consecutive detections, obtained at any particular value of y^*, was maximum when $(U_c \Delta t)/L = 3.4$ (in general, times are converted to distances by multiplying with U_c, an average convection velocity of the structures, discussed later). Similarly, when the movable probe was at $y^* > 0$ and the fixed rake was at $y^* < 0$, the probability density function of Δt for detections in the temperature signal from the movable probe, relative to detections in the fixed-rake signals, was maximum when $(U_c \Delta t)/L \approx \pm 1.7$. Therefore, the data for $y^* \leqslant 0$ were searched to find detections which were simultaneously preceded and followed by detections with time delays of ± 3.4, while for $y^* > 0$ the data were searched for fixed rake detections that were preceded and followed by movable-probe detections with time delays of $\approx \pm 1.7$. There were about 500 ($= n$) groups of three detections for each y^* location (fewer for the largest $|y^*|$ values), and taken together, the resulting conditional averages yield the antisymmetrical arrangement of structures used in our further analysis.

The average frequency of occurrence of the structures was about 130 Hz at

$x/d = 420$. This corresponds to about 0.3 of the cylinder Strouhal frequency. This structure frequency decreased approximately linearly from $x/d = 180$ to $x/d = 800$. Correspondingly the ratio of the average wavelength of the far-wake structures to the wavelength of the Kármán vortex street increased almost linearly with x/d. Details of this variation are given in Antonia, Browne & Fulachier (1987).

4. Topology of structures

4.1. *Velocity vectors*

The velocity-vector plot in figure 3 was obtained in a manner fully described in Antonia *et al.* (1986) for a jet and in Browne *et al.* (1986) for a wake. It is similar to that used in the near-wake studies (Cantwell & Coles 1983; Hayakawa & Hussain 1985; Kiya & Matsumura 1985). Once $\langle U \rangle$ and $\langle V \rangle$ are estimated, the corresponding velocity vector in the (x, y)-plane can be displayed in a frame of reference moving with a velocity U_c. Cantwell (1979) and Coles (1982) emphasized the importance of selecting U_c correctly since in general the pattern of streamlines or particle paths will depend on U_c. There is considerable dispersion in reported estimates of U_c in the near wake: $0.755U_1$ (Cantwell & Coles 1983), $0.875U_1$ (Hayakawa & Hussain 1985) and $0.92U_1$ (Kiya & Matsumura 1985). One would however expect the dispersion to be smaller in the far wake since the mean velocity defect decreases as x/d increases. At $x/d = 420$, a range of U_c values was tried and for each U_c, conditional velocity vectors, obtained relative to an observer moving at a velocity of U_c, were obtained. When these velocity vectors were plotted, the average centreline of the resulting structures appeared to be at $y^* = 0.9$ with a corresponding U_c of 6.52 m/s or $0.97U_1$.

Conditional velocity vectors, obtained relative to an observer moving with this U_c, are shown in figure 3 in the plane Δx^* *vs.* y^*. In figure 3, $\Delta x^* = -(\tau U_c)/L$, where τ is the time measured from the detection instants. Positive values of Δx^* refer to locations downstream of the detection locations (or times earlier than the instants of detection). The same scales are used for Δx^* and y^* to avoid possible distortion of the pattern in this and subsequent figures.

Figure 3 shows a succession of rotating patterns with a scale of about one half-width in either the Δx^* or y^* direction. Associated with these patterns are alternating critical points (e.g. Cantwell 1979) located at $|y^*| \approx 1$ on either side of the centreline. These points can be identified as centres and saddles and are denoted in figure 3 and subsequent figures by the letters C and S respectively. Centres can, to a first approximation, be identified with the centroids of the clockwise and counterclockwise patterns while saddles lie at the intersections of diverging and converging separatrices which separate neighbouring patterns. The diverging separatrices are indicated (figure 3 and subsequent figures) by arrows directed away from the saddle points. Converging separatrices (not shown) are directed towards the saddle point and are approximately orthogonal to the diverging separatrices.

4.2. *Streamlines*

Streamlines shown in figure 4 associated with the velocity-vector pattern in figure 3 were obtained by calculating the stream function $\langle \Psi \rangle$ for the same frame of reference as figure 3. In this reference frame, $\langle \Psi^* \rangle$ is quasi-steady and is a solution of the differential equation $\mathrm{d}\langle \Psi^* \rangle = \langle U^* \rangle \,\mathrm{d}y^* - \langle V^* \rangle \,\mathrm{d}x^*$. For a streamline ($\langle \Psi^* \rangle =$ const) to exist, continuity must be satisfied, i.e. $\partial \langle U^* \rangle / \partial x^*$ should equal $-\partial \langle V^* \rangle / \partial y^*$. The data for $\langle U^* \rangle$ and $\langle V^* \rangle$ generally met this condition except in the vicinity of the temperature fronts (diverging separatrices) where non-zero values

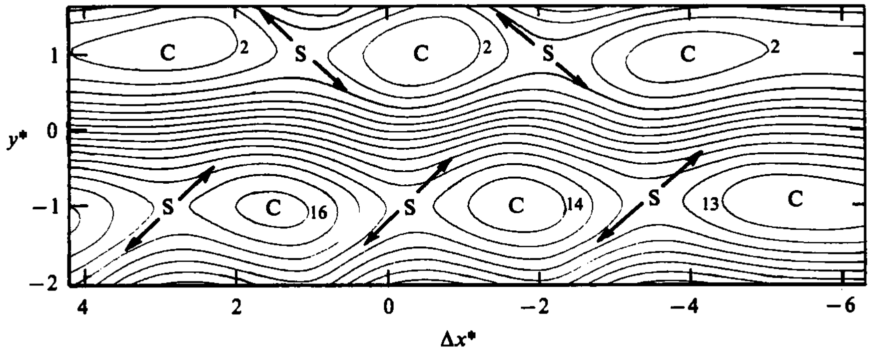

FIGURE 4. Stream functions for the coherent motion relative to an observer moving right to left with a convection velocity U_c. (Contour step = 0.05.)

may result from large gradients, with respect to either x^* or y^*, in these regions and perhaps from non-zero values of $\partial\langle W^*\rangle/\partial z^*$. In this sense, the streamlines in figure 4 may be slightly inaccurate near diverging separatrices.

A first approximation for $\langle\Psi^*\rangle$ was calculated using

$$\langle\Psi^*\rangle = \int_{y_0^*}^{y^*} (\langle U^*\rangle - U_c^*)\,dy^* - \int_{x_0^*}^{x^*} \langle V^*\rangle\,dx^*$$

for a particular choice of (x_0^*, y_0^*). This approximation was then improved by comparing $\partial\langle\Psi^*\rangle/\partial y^*$ with $\langle U^*\rangle - U_c^*$ and $\partial\langle\Psi^*\rangle/\partial x^*$ with $-\langle V^*\rangle$. A few iterations were required before the initial dependence on (x_0^*, y_0^*) disappeared and acceptable convergence for $\langle\Psi^*\rangle$ was achieved. As expected, figure 4 reflects the information contained in figure 3. Closed contours of $\langle\Psi^*\rangle$ near centres are elliptical and elongated in the streamwise direction. The oscillatory behaviour of $\langle\Psi^*\rangle$ on either side of the flow centreline reflects the antisymmetry of the selected group of structures.

4.3. *Vorticity and strain rate*

In the near-wake investigations, regions surrounding centres have a high coherent spanwise vorticity while saddles mark regions which have large coherent strain rates. The spanwise component of the vorticity vector is given by $\partial\langle V^*\rangle/\partial x^* - \partial\langle U^*\rangle/\partial y^*$, and the coherent strain rate is given by $\partial\langle U^*\rangle/\partial y^* + \partial\langle V^*\rangle/\partial x^*$. These two quantities were calculated from the present data for $\langle U^*\rangle$ and $\langle V^*\rangle$ and the resulting contours for the larger values of each, slightly smoothed, are presented in figure 5. Maxima of the spanwise vorticity occur approximately at centres whereas maxima of the strain rate are close to the saddle locations. The position and the shape of the vorticity contours are similar to those of the closed $\langle\Psi^*\rangle$ contours in figure 4. Strain-rate contours (figure 5) are elliptical in shape but their major axis is generally aligned with the diverging separatrix, in contrast with the nearly streamwise alignment of the spanwise vorticity contours.

4.4. *Intermittency*

It is of interest to relate the location of coherent structures to the boundary between turbulent and non-turbulent fluid. An indication of this boundary is provided by contours of $\langle I\rangle$, the conditionally averaged intermittency function. Here, I is defined as unity (turbulent region) when the instantaneous temperature exceeds a certain threshold; I is zero (non-turbulent region) otherwise. To estimate

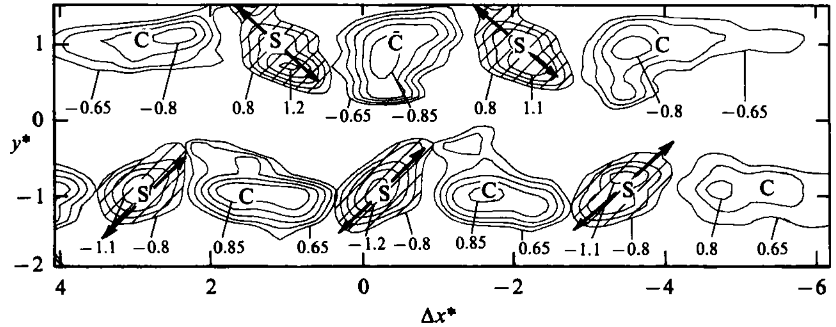

FIGURE 5. Contours of spanwise vorticity and strain rate due to the coherent motion. Plain contours: spanwise vorticity, $\partial\langle V^*\rangle/\partial x^* - \partial\langle U^*\rangle/\partial y^*$. Cross-hatched contours: strain rate, $\partial\langle U^*\rangle/\partial y^* + \partial\langle V^*\rangle/\partial x^*$.

the threshold, two methods were used. In one method, I is compared with temperature signals such as those shown in figure 2 (the conventional intermittency factor $\bar{I}$ is 0.5). The threshold is fine tuned until a visually satisfactory comparison is achieved. The second method is essentially based on the approach described by Bilger, Antonia & Sreenivasan (1976). It consists in plotting the cumulative probability of temperature and identifying the threshold with the location at which the probability departs from the Gaussian behaviour expected for a temperature signal in the non-turbulent region. The first method was preferred for relatively small values of $|y^*|$, typically in the range 0.8–1.2, while the second was employed at larger $|y^*|$ (1.2–2.0).

Contours in figure 6(*a*) indicate that the magnitude of $\langle I\rangle$ is not very different (close to unity) at centres and saddles. This contrasts with the observations of Cantwell & Coles (1983) who note that centres can be detected in terms of a maximum for $\langle I\rangle$ whereas saddles are close to a minimum for $\langle I\rangle$. Kiya & Matsumura's (1985) $\langle I\rangle$ contours exhibit a maximum at centres but the local minimum in $\langle I\rangle$ is slightly, but consistently, offset from their reported saddle positions. The present contours are more like those of Kiya & Matsumura, except that the centreplane region is fully turbulent for the far wake.

Both the near-wake contours and the present contours suggest that the saddle plays an important role in the entrainment of potential fluid. The contours of figure 6(*a*) suggest that this entrainment occurs near the downstream boundary of a region associated with large spanwise vorticity. The upstream boundary is associated with relatively warmer turbulent fluid moving away from the centreline: contours for relatively large values of $\langle I\rangle$ are stretched towards large values of $|y^*|$ along the diverging separatrix. Contours of $\langle T^*\rangle$, figure 6(*b*), are, not surprisingly, quite similar to the intermittency contours in figure 6(*a*). Figure 6(*b*) emphasizes the way warm fluid is stretched outwards along the diverging separatrix or temperature front, towards the edge of the wake. Similarly, cold fluid is carried along the same front towards the centreline. Note also how the constant-temperature lines are closely grouped near saddles and widely separated near centres.

5. Contributions from large-scale and small-scale motions

In this section, we focus on the topologies of normal and shear stresses and of the temperature variance and heat fluxes associated with the coherent large-scale motions and with the small-scale motions. We also present results for the production

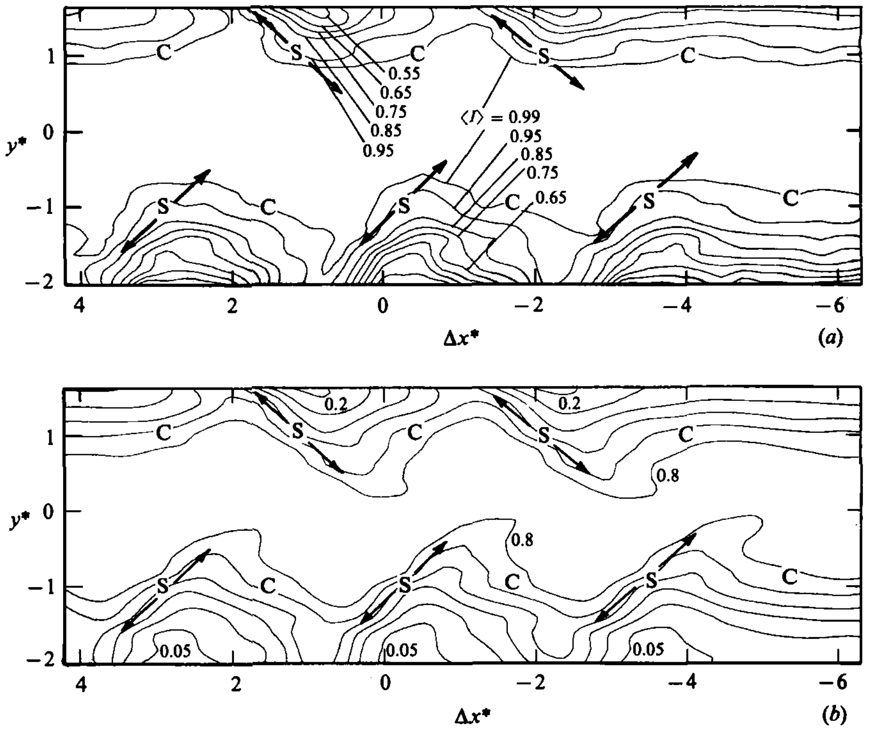

FIGURE 6. Contours of intermittency and temperature associated with the large-scale motion. (*a*) $\langle I\rangle$. Except for $\langle I\rangle = 0.99$, contours are shown at intervals of 0.1. (*b*) $\langle T^*\rangle$. Contours are shown at intervals of 0.15.

and part of the dissipation terms for the kinetic energy and temperature variance of the small-scale motion. For reasons given in §3, we use the triple decomposition for resolving contributions, from the large-scale and small-scale motions, to the normal and shear stresses as well as to the temperature variances and heat fluxes.

5.1. *Velocity and temperature variances*

Results for the normal stresses and temperature variance are shown in figure 7 (large scale) and figure 8 (small scale). The largest values of $\tilde{U}^{*2}$, $\tilde{V}^{*2}$, $\tilde{T}^{*2}$ occur neither at centres nor saddles. They are found along the diverging separatrices on either side and at approximately the same distance from the saddle point. These extrema are generally of similar magnitude except for $\tilde{T}^{*2}$, where the highest values occur at the largest values of $|y^*|$. Note that the contours of $\tilde{U}^{*2}$ and $\tilde{T}^{*2}$ have similar orientations, the major axes of the ellipses being inclined at about 45° to the centreline. The major axes of the $\tilde{V}^{*2}$ contours tend to be almost perpendicular to the centreline.

There is obviously more dispersion in figure 8 than in figure 7. This is not surprising since the quantity $\langle F_s^2\rangle$ is formed, using (2), by subtracting $\tilde{F}^2$ from $\langle (F-\overline{F})^2\rangle$. Since the population of detections, from which $\tilde{F}$ is determined, is associated with structures whose durations and amplitudes may vary slightly, the resulting value of $\langle F_s^2\rangle$ will inevitably reflect these differences (as noted by Cantwell & Coles 1983). Also, as one moves away from the detection instant, i.e. as $|\Delta x^*|$ increases, the accuracy of $\tilde{F}$ is impaired (this can be seen in all figures showing contours of quantities associated with $\tilde{F}$) with further impairment in the accuracy of $\langle F_s^2\rangle$.

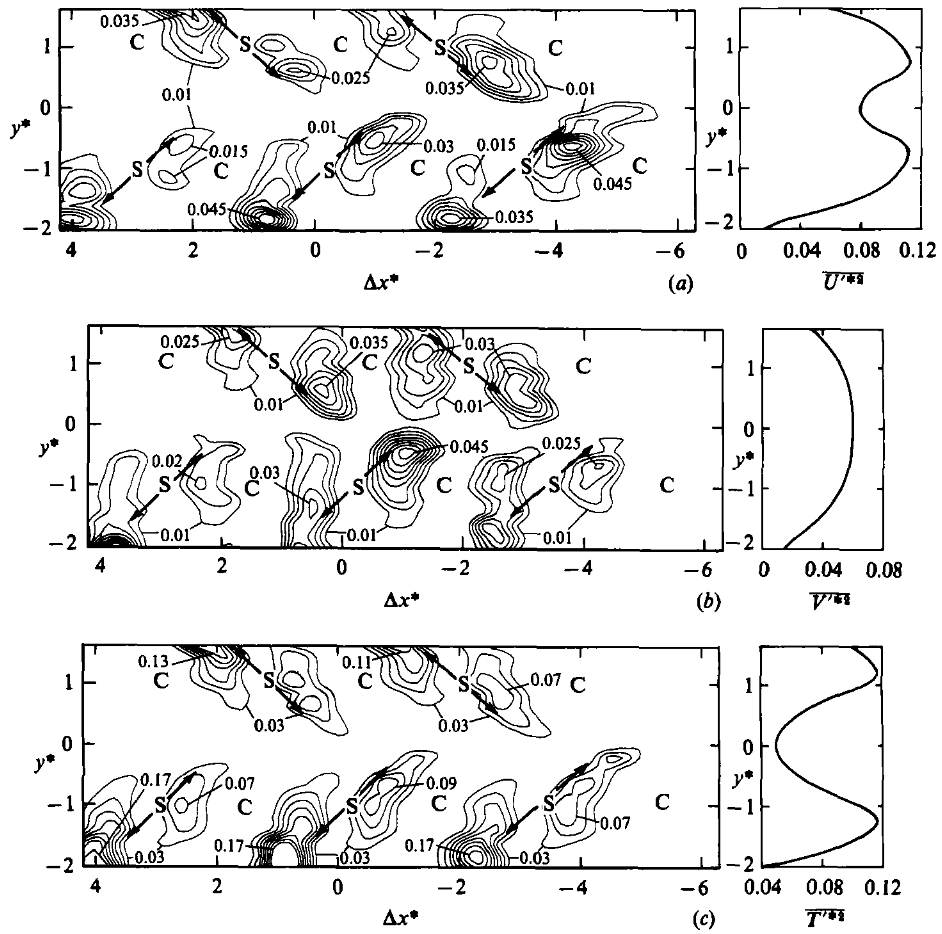

FIGURE 7. Contours of normal stresses and temperature variance due to the large-scale motion. (a) $\tilde{U}^{*2}$; (b) $\tilde{V}^{*2}$; (c) $\tilde{T}^{*2}$. The curves are distributions of Reynolds averaged normal stresses and temperature variance.

Notwithstanding the previous remarks, contours of $\langle U_s^{*2} \rangle$, $\langle V_s^{*2} \rangle$ and $\langle T_s^{*2} \rangle$ (figure 8) exhibit significant spatial coherence at least for a relatively small range of $|\Delta x^*\rangle$. We also note that the relative differences between these three sets of contours are more important than those in figure 7. In particular, there are relatively large concentrations of $\langle U_s^{*2} \rangle$ near centres but significant values are also found close to the centreline. The peak values in figure 8(*a*) are larger than those in figure 7(*a*) by a factor of about 3. For $\langle V_s^{*2} \rangle$, the largest concentrations occur inside a narrow region on either side of the centreline (figure 8*b*). In the case of $\langle T_s^{*2} \rangle$ (figure 8*c*), the highest values reside along the diverging separatrices but non-negligible contributions can also be detected near centres. It is of interest to compare the locations and magnitudes of the contours in figures 7 and 8 with those of the Reynolds-averaged distributions for $\overline{U'^{*2}}$, $\overline{V'^{*2}}$ and $\overline{T'^{*2}}$. The latter distributions are shown in figures 7 and 8 to facilitate comparison with the contour values. These distributions peak at $|y^*| \approx 0.8$, 0 and 1.2 respectively. The difference in these locations is reflected, qualitatively at least, in the spatial locations of the contours in figure 7 and especially figure 8.

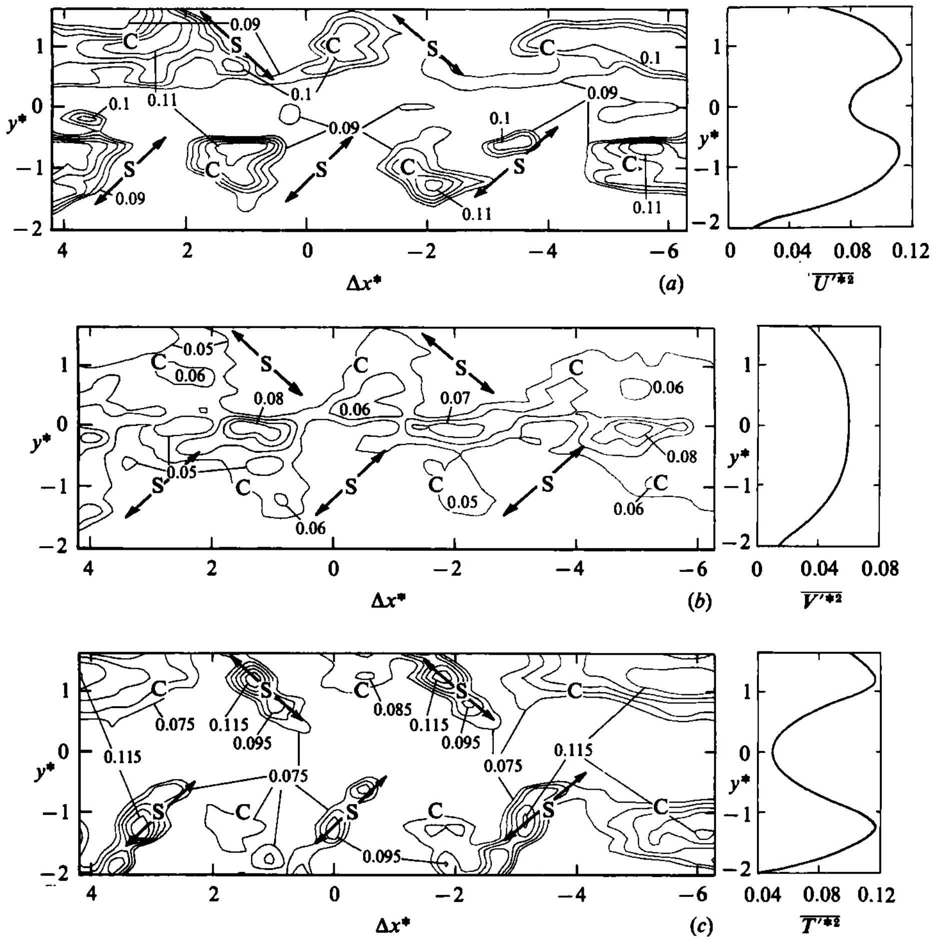

FIGURE 8. Contours of normal stresses and temperature variance due to the small-scale motion. (*a*) $\langle U_s^{*2}\rangle$; (*b*) $\langle V_s^{*2}\rangle$; (*c*) $\langle T_s^{*2}\rangle$. The curves are distributions of Reynolds averaged normal stresses and temperature variance.

5.2. *Momentum and heat transport*

Contours of $\tilde{U}^*\tilde{V}^*$, $\tilde{U}^*\tilde{T}^*$, $\tilde{V}^*\tilde{T}^*$, not shown here, are very similar in appearance to the contours of $\tilde{U}^{*2}$, $\tilde{V}^{*2}$, $\tilde{T}^{*2}$ (figure 7). Whereas $\tilde{U}^*\tilde{V}^*$ contours are larger in magnitude near the centreline than in the outer wake, $\tilde{U}^*\tilde{T}^*$ and $\tilde{V}^*\tilde{T}^*$ contours had their largest values in the region $|y^*| > 1$. The latter observation reflects the relative magnitudes of the temperature-variance contours of figure 7 (*c*). Shear stresses and heat fluxes associated with the small-scale motion tend to have larger magnitudes near centres although, in the case of $\langle U_s^* T_s^*\rangle$ and $\langle V_s^* T_s^*\rangle$, significant values are observed near saddle points.

Contributions of the large-scale and small-scale motions to the Reynolds-averaged shear stress and heat fluxes were estimated by computing the ratios $\overline{\tilde{F}\tilde{G}}/\overline{F'G'}$ and $\overline{F_s G_s}/\overline{F'G'}$ (see (5)). Only the former values are shown in table 1, since (5) was closely verified at each y^*. The large-scale motion makes a larger contribution to $\overline{V'T'}$ than to $\overline{U'V'}$, suggesting that the transport of heat is carried out more effectively than that of momentum, especially at large y^*. Also included in the table are the

y^*	$\overline{\tilde{U}\tilde{V}}/\overline{U'V'}$	$\overline{\tilde{U}\tilde{T}}/\overline{U'T'}$	$\overline{\tilde{V}\tilde{T}}/\overline{V'T'}$	$\overline{\tilde{U}^2}/\overline{U'^2}$	$\overline{\tilde{V}^2}/\overline{V'^2}$	$\overline{\tilde{T}^2}/\overline{T'^2}$
0	—	0.18	—	0.05	0.04	0.20
0.2	0.25	0.16	0.37	0.05	0.10	0.21
0.4	0.26	0.23	0.43	0.07	0.20	0.23
0.6	0.27	0.27	0.45	0.09	0.21	0.28
0.8	0.28	0.30	0.45	0.09	0.22	0.32
1.0	0.28	0.30	0.45	0.09	0.22	0.33
1.2	0.28	0.30	0.44	0.09	0.22	0.33
1.4	0.28	0.32	0.45	0.10	0.22	0.36
1.6	0.28	0.36	0.48	0.14	0.26	0.40
1.8	0.26	0.41	0.50	0.18	0.26	0.45
2.0	0.27	0.45	0.53	0.20	0.25	0.48

TABLE 1. Contribution of the large-scale motion to Reynolds-averaged stresses, heat fluxes and temperature variance

contributions of the large-scale motion to the Reynolds normal stresses and the temperature variance. The contributions to the normal stresses are quite small near the centreline and increase only slightly with y^*. The contribution from $\overline{\tilde{T}^2}$ becomes significant at large y^*, which is consistent with the importance of the coherent heat fluxes in this region.

5.3. *Production and dissipation*

Both Cantwell & Coles (1983) and Hayakawa & Hussain (1985) presented estimates for the production $\langle P_E \rangle$ of energy associated with the small-scale motion. This term, which is also an energy sink for the large-scale motion, is given by

$$\langle P_E \rangle = -\langle U_s^2 \rangle \frac{\partial \langle U \rangle}{\partial x} - \langle V_s^2 \rangle \frac{\partial \langle V \rangle}{\partial y} - \langle U_s V_s \rangle \left(\frac{\partial \langle U \rangle}{\partial y} + \frac{\partial \langle V \rangle}{\partial x} \right). \tag{7}$$

The three terms on the right-hand side of (7) were calculated and their normalized sum $\langle P_E^* \rangle$ is shown in figure 9(*a*). Although the individual terms are not shown, they do not all exhibit the same spatial features as the sum. The first term shows positive contributions along the diverging separatrix but marginally smaller negative contributions near centres. The second term is largest in a relatively narrow region $-0.5 \lesssim y^* \lesssim 0.5$ where $\langle V_s^2 \rangle$ is large and the gradient $\partial \langle V \rangle / \partial y$ is also significant. The third term provides a positive contribution, comparable in magnitude with that of the first term, along the diverging separatrix. When the three terms are added, the additive positive contributions along the diverging separatrix overwhelm the 'sink' of energy which exists near the centres, due mainly to $-\langle U_s^2 \rangle \, \partial \langle U \rangle / \partial x$. Since the smallest contours are not shown in figure 9(*a*), the negative contributions near centres do not appear.

The production $\langle P_\theta \rangle$ of the temperature variance associated with the small-scale motion can be obtained by writing the transport equation for $\langle T_s^2 \rangle$. The expression for $\langle P_\theta \rangle$ is

$$\langle P_\theta \rangle = -\langle U_s T_s \rangle \frac{\partial \langle T \rangle}{\partial x} - \langle V_s T_s \rangle \frac{\partial \langle T \rangle}{\partial y}. \tag{8}$$

Each term on the right-hand side was calculated and found to be significantly positive along the diverging separatrix. Although the second term exhibits a significant positive contribution near centres, due to the concentration of $\langle V_s T_s \rangle$ in these regions, the normalized sum $\langle P_\theta^* \rangle$ (figure 9*b*) emphasizes mainly the contribution

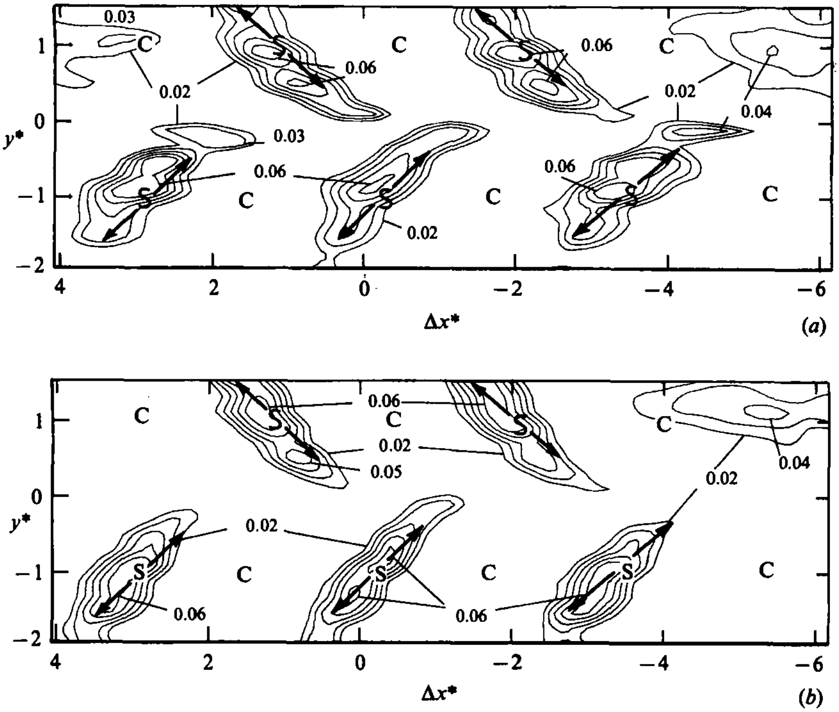

FIGURE 9. Contours of the production of turbulent energy (*a*) and temperature variance (*b*) for the small-scale motion. (*a*) $-\langle U_s^{*2}\rangle\,\partial\langle U^*\rangle/\partial x^*-\langle V_s^{*2}\rangle\,\partial\langle V^*\rangle/\partial y^*-\langle U_s^*\,V_s^*\rangle\,[\partial\langle U^*\rangle/\partial y^*+\partial\langle V^*\rangle/\partial x^*]$. (*b*) $-\langle U_s^*\,T_s^*\rangle\,\partial\langle T^*\rangle/\partial x^*-\langle V_s^*\,T_s^*\rangle\,\partial\langle T^*\rangle/\partial y^*$.

along the diverging separatrix. The behaviour of $\langle P_\theta^*\rangle$ (figure 9*b*) is similar to that of $\langle P_E^*\rangle$ (figure 9*a*).

To obtain some idea of how the dissipations of energy and temperature variance associated with the small-scale motion are distributed spatially, one component only of these terms was calculated (figure 10). Estimates of $\langle(\partial U_s/\partial x)^2\rangle$ and $\langle(\partial T_s/\partial x)^2\rangle$ were obtained by evaluating the right-hand side of the equation

$$\left\langle\left(\frac{\partial F_s}{\partial t}\right)^2\right\rangle=\left\langle\left(\frac{\partial F}{\partial t}\right)^2\right\rangle-\left(\frac{\partial\langle F\rangle}{\partial t}\right)^2\quad(F\equiv U\text{ or }T)$$

and using the space–time transformation $\partial/\partial x\equiv-U_c^{-1}\,\partial/\partial t$. The resulting distribution of $\langle(\partial T_s^*/\partial x^*)^2\rangle$ (figure 10*b*) shows much the same behaviour as that of $\langle P_\theta^*\rangle$; the contours corresponding to large values of $\langle(\partial T_s^*/\partial x^*)^2\rangle$ stretch out in the direction of the diverging separatrices to relatively large values of y^*. In the case of $\langle(\partial U_s^*/\partial x^*)^2\rangle$, contours do not stretch to large $|y^*|$ but there is a reasonable indication that the largest values of this quantity are also directed along the diverging separatrices.

6. Comparison with the organized motion in the near wake

The most salient features in the previous figures are summarized in figure 11 to permit an overview of the flow topology and a comparison with the toplogy of the near wake.

The centres are associated with high coherent spanwise vorticity and lie on a line

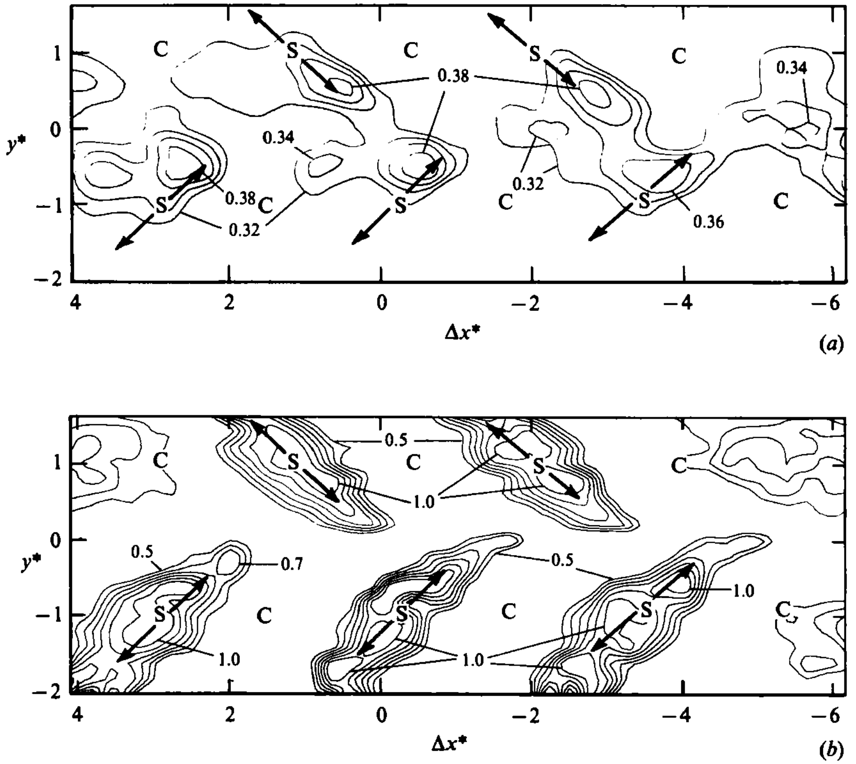

FIGURE 10. Contours of one component of the dissipation of turbulent energy (*a*) and temperature variance (*b*) for the small-scale motion. (*a*) $\langle(\partial U_s^*/\partial x^*)^2\rangle$; (*b*) $\langle(\partial T_s^*/\partial x^*)^2\rangle$.

where the coherent intermittency is nearly unity, i.e. in the fully turbulent part of the flow. At centres, high concentrations can be found for some but not all quantities associated with the small-scale motion. For example, $\langle U_s^2\rangle$ and $\langle U_s V_s\rangle$ are large there but there are also important concentrations of $\langle U_s V_s\rangle$ in the saddle regions and $\langle V_s^2\rangle$ is especially large in a region close to the centreline. The temperature variance $\langle T_s^2\rangle$ is conspicuously high along the diverging separatrices near saddles. Saddles are unambiguously identified by large strain rates for the large-scale motion. They are also associated with large values of the production of kinetic energy and temperature variance of the small-scale motion. Large values of normal and shear stresses, temperature variance and heat fluxes associated with the large-scale motion occur neither at centres nor at saddles but in two confined regions of space located on either side of a saddle, approximately in the direction of the diverging separatrix.

There is significant qualitative similarity between the present topology and that obtained in the near wake. There are however differences: those listed below relate to both the locations of centres and saddles and the domains of importance of some of the turbulence quantities that have been considered.

(i) For the near wake, the difference in mean y-locations of centres and saddles can be significant. Near the cylinder, centres are nearly on the centreline (e.g. figure 1). As the distance from the cylinder increases, the lateral distance of the centre from the centreline increases. The double row of vortices in the far wake contrasts with the single row in the near wake.

(ii) Instantaneous spanwise vorticity maps presented by Hayakawa & Hussain

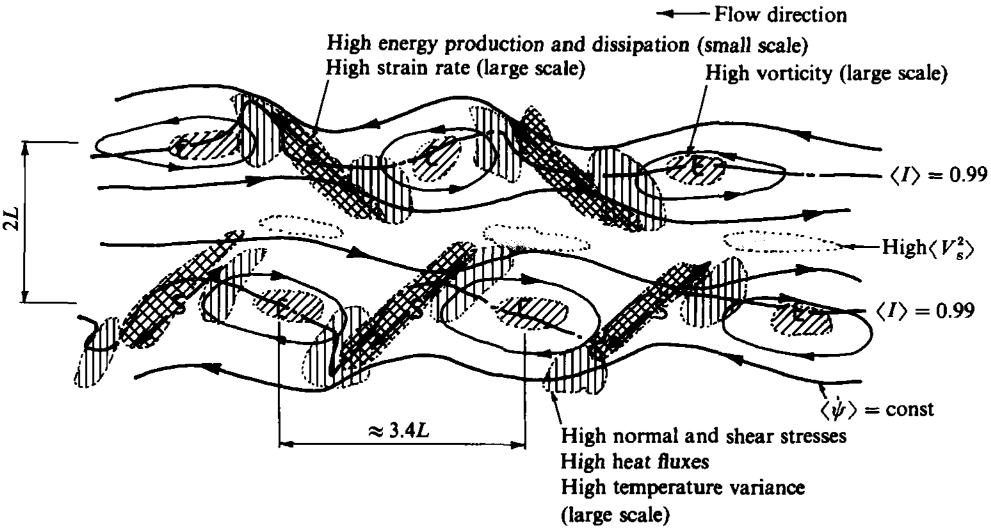

FIGURE 11. Summary sketch of far-wake topology. —▶—, $\langle \Psi^* \rangle$ = constant; – – –, $\langle I\rangle = 0.99$. ▨, high vorticity (large scale); ▩, high energy production/dissipation (small scale), high strain rate (large scale); ▥, high normal and shear stresses, heat fluxes and temperature variances (large scale).

(1985) indicate that the vorticity boundary associated with each centre extends significantly across the centreline. This is much less pronounced in the far wake.

(iii) Cantwell & Coles (1983) observed that centres could, *inter alia*, be identified with a peak in the intermittency while saddles appeared to lie on the boundary $\langle I\rangle = 0.5$. Neither observation is valid for the far wake (figures 6 and 11).

(iv) Cantwell & Coles (1983) noted that a centre could be detected in terms of a peak in kinetic energy for the small-scale motion. For the far wake, there are important concentrations of normal stresses, associated with the small-scale motion, near centres but there are also significant concentrations, especially in $\langle V_s^2\rangle$, close to the flow centreline. This evidence does not fully support Coles' (1982) premise for free turbulent shear flows that, following its generation at saddles, the small-scale turbulence is transported to centres. We also find that $\langle U_s V_s\rangle$ is more dominant near centres than near saddles. This contrasts with Hayakawa & Hussain's (1985) near-wake observation that the shear stress associated with the small-scale motion was largest at saddle points.

In both the near wake and the far wake, the saddle region is important in terms of both the production of turbulent energy and the entrainment of irrotational fluid. Cantwell & Coles (1983) conjectured that turbulence production near saddles is 'carried out primarily by stretching of small-scale vorticity oriented along the diverging separatrices'. The present production contours (figure 9) are consistent with this conjecture and although only one component of the dissipation has been measured (figure 10), the implication is that dissipation is large in regions where the production is large. The close similarity between production and dissipation of kinetic energy and temperature variance for the small-scale motion is not reflected in the spatial distributions (figure 8) of $\langle U_s^2\rangle$, $\langle V_s^2\rangle$ and $\langle T_s^2\rangle$. Although we have not measured $\langle W_s^2\rangle$ and cannot therefore directly compare $\langle T_s^2\rangle$ with the small-scale kinetic energy, similarity between these latter two quantities seems unlikely, especially in view of the high concentrations of $\langle T_s^2\rangle$ along diverging separatrices.

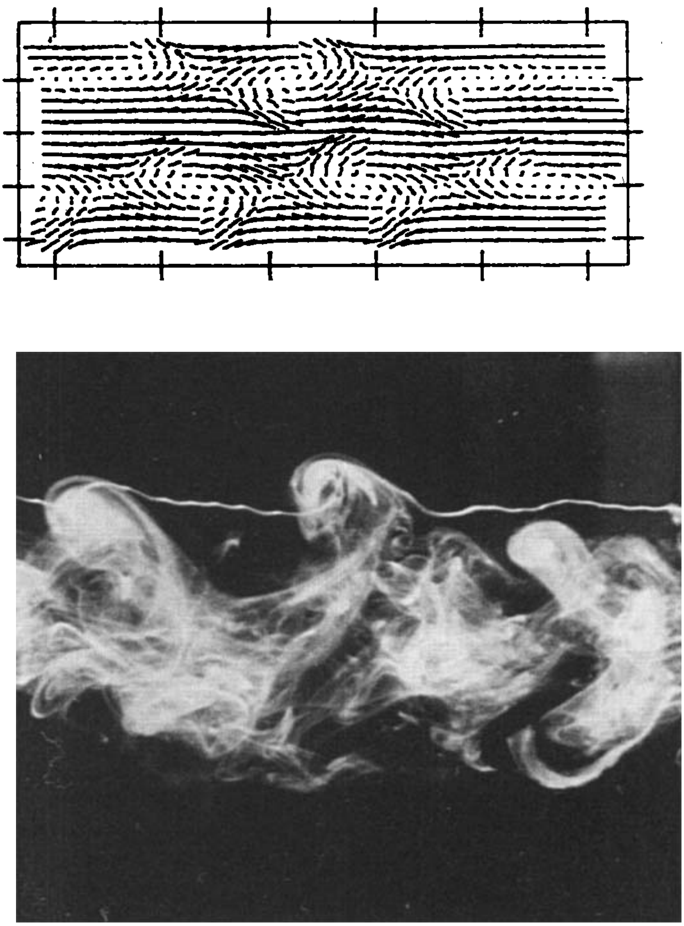

FIGURE 12. Photograph showing a group of dye bulges with approximately the same streamwise spacing as used in the topology. (The velocity-vector plot of figure 3 is reproduced in the upper half of the figure.) The flow is right to left ($R_d = 430$, the central bulge is at $x/d \approx 240$).

7. Relation between topology and the physics of the flow

An accurate interpretation of figure 11, in terms of the physics of the flow, is not possible since what has been presented is a two-dimensional cut through a three-dimensional structure. To provide some insight into the nature of this three-dimensional structure, we present below some flow-visualization results.

The photograph shown in figure 12 contains a group of bulges which occur at approximately the same streamwise wavelength as the group of detections used to construct the present topology. The bulges are marked by a significant concentration of dye (our observations, with the eye following the motion of the bulges, indicated that the dye concentrations rotate about an axis in the z-direction, suggesting that the bulges have a spanwise vorticity component). The tips of the bulges have a tendency to curl over in the direction of the centreline. The back of a bulge can be identified with the dye boundary which is at approximately 45° to the centreline. Cantwell & Coles (1983), referring to a schlieren photograph of Thomann (1959), suggested that the direction of the separatrix was made visible by the presence of strong density gradients. Our dye photographs (e.g. figure 12) support this suggestion; the association of the dye boundary (high concentration gradients) with the diverging separatrix mirrors the association of the temperature front (high temperature gradients) with the diverging separatrix.

We have included in figure 12 a suitably scaled representation of the vector plots (figure 3) for comparison with the dye photograph. A rigorous comparison is obviously not possible since the vector pattern is an average over a large number of bulges while the photograph shows streaklines associated with a few bulges. The general lack of equivalence, in unsteady flow, between streaklines and streamlines is also an obstacle to the comparison. Nevertheless, there is reasonable similarity between the two representations in figure 12. Centres in the photograph can be loosely identified with the centroids of regions with a large dye concentration. Interestingly, the upper dye streakline (introduced in the irrotational flow) is temporarily drawn into the central bulge (it can loosely be interpreted as an instantaneous streamline or pathline) and curls around so that its slope becomes indeterminate, presumably at the centre. Although it is difficult to locate saddle points precisely on the photograph in figure 12, it seems reasonable to identify them with the nearly orthogonal intersection of the dye separatrices† (e.g. on the back of the central bulge). A similar observation was made by Perry, Chong & Lim (1982) with reference to the smoke-dye patterns of Zdravkovich (1969).

Previous studies of the far wake have pointed to the existence of two main types of vortical structures: double-roller eddies (e.g. Grant 1958; Payne & Lumley 1967; Townsend 1976; Mumford 1983; Savill 1983) and spanwise eddies (Keffer 1965; Townsend 1979; Mumford 1983). The former are aligned in the plane of main shear and contain significant streamwise vorticity while the latter have spanwise vorticity. The possibility that these two eddy types are connected so that the spanwise eddies join the double-roller eddies at their outer ends has been mentioned by Roshko (1976), Coles (1982) and discussed by Mumford (1983). Some evidence in support of this possibility is provided by figure 13. For this photograph, the dye streakline was introduced in the tunnel contraction upstream of the cylinder and was drawn into the turbulent wake some 180 diameters downstream of the cylinder. At least initially, the dye remains relatively organized, delineating a set of bulges on either side of the flow centreline. Each bulge comprises a succession of dye loops, the extremities of which tend to curl over towards the centreline. Since what is observed is the response of the dye to the vortices rather than the vortices themselves, it is difficult to associate unambiguously the dye loops in the photograph (figure 13) with vortical structures. With artistic licence, we have sketched in the inset of the photograph a possible vortical structure: such a structure, reminiscent of a hairpin vortex, contains both spanwise vorticity associated with its tip, and streamwise vorticity associated with its legs. The legs tend to be stretched in a plane aligned, on average, with the direction of the diverging separatrix. The vortex model depicted in figure 13 is consistent with both Roshko's (1976) conjecture that double-roller eddies and spanwise eddies are two mutually perpendicular views of a vortex loop and with Coles' (1982) conjecture that the characteristic of a turbulent far wake is probably a vortex loop closed across the wake. We have not closed the legs of the model vortex as we do not know how to do this (the dye information is not helpful since a streakline cannot be broken).

Although there is general similarity between the topological features of figure 11 and the photographs of figures 12 and 13, it is clear that figure 11 represents a

---

† This is more easily observed in the near wake (figure 1).

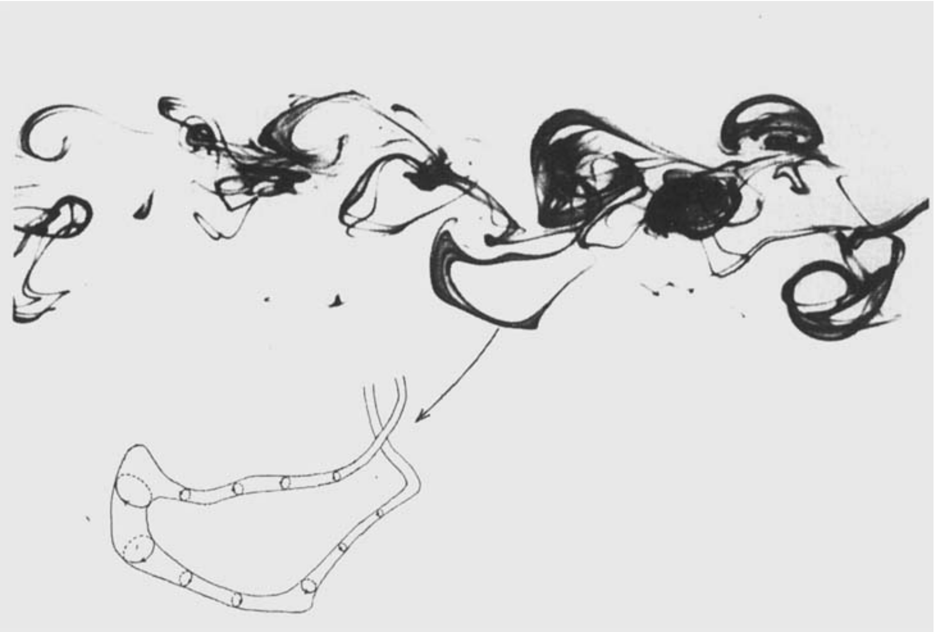

FIGURE 13. Single dye streakline entrained into the far wake. The flow is right to left ($R_d = 280, 180 \lesssim x/d \lesssim 300$).

simplified cut through three-dimensional bulges, each of these possibly comprising clusters of vortex loops or hairpin vortices. The manner in which the bulges originate, the way in which the vortices interact with each other or how they terminate in the flow are matters for future investigation. It should also be noted that the present measurements and flow visualizations were made at small Reynolds numbers. Although the flow visualizations of Papailiou & Lykoudis (1974) and Wlezien (1981) confirmed the presence of the large structures in the far wake at larger Reynolds numbers, it would be useful to extend the present topology to larger Reynolds numbers, especially with a view to establishing the importance of the far-wake structures with respect to their strength (e.g. energy content) and their contribution to momentum and heat transport. Since the Kármán street is also expected to decay more rapidly as the Reynolds number increases, a higher R_d investigation may shed some light on the possible interrelation between the near-wake and far-wake regions.

The support of the Australian Research Grants Scheme is gratefully acknowledged. We are grateful to M. Astier and A. Morand for their contributions to the flow visualizations.

REFERENCES

ANTONIA, R. A., BROWNE, L. W. B. & FULACHIER, L. 1987 Average wavelength of organised structures in the turbulent far wake. *Expts Fluids* **5** (in press).

ANTONIA, R. A., CHAMBERS, A. J., BRITZ, D. & BROWNE, L. W. B. 1986 Organized structures in a turbulent plane jet: topology and contribution to momentum and heat transport. *J. Fluid Mech.* **172**, 211–229.

BARSOUM, M. L., KAWALL, J. G. & KEFFER, J. F. 1978 Spanwise structure of the plane turbulent wake. *Phys. Fluids* **21**, 157–161.

BEVILAQUA, P. M. & LYKOUDIS, P. S. 1978 Turbulence memory in self-preserving wakes. *J. Fluid Mech.* **89**, 589–606.

BILGER, R. W., ANTONIA, R. A. & SREENIVASAN, K. R. 1976 The determination of intermittency from the probability density function of a passive scalar. *Phys. Fluids* **19**, 1471–1474.

BROWNE, L. W. B. & ANTONIA, R. A. 1986 Reynolds shear stress and heat flux measurements in a cylinder wake. *Phys. Fluids* **29**, 709–713.

BROWNE, L. W. B., ANTONIA, R. A. & BISSET, D. K. 1986 Coherent structures in the far-field of a turbulent wake. *Phys. Fluids* **29**, 3612–3617.

BUDNY, R. S., KAWALL, J. G. & KEFFER, J. F. 1979 Vortex street evolution in the wake of a circular cylinder. *Proc. Second Symp. on Turbulent Shear Flows*, Imperial College, London, pp. 7.20–7.25.

CANTWELL, B. J. 1979 Coherent turbulent structures as critical points in unsteady flow. *Arch. Mech.* **31**, 707–721.

CANTWELL, B. & COLES, D. 1983 An experimental study of entrainment and transport in the turbulent near wake of a circular cylinder. *J. Fluid Mech.* **136**, 321–374.

CIMBALA, J. M. 1984 Large structure in the far wake of two-dimensional bluff bodies. Ph.D. thesis, California Institute of Technology.

CIMBALA, J. M. 1985 An experimental study of large structures in the far wakes of two-dimensional bluff bodies. *Proc. Fifth Symp. on Turbulent Shear Flows*, pp. 4.1–4.6. Cornell University.

COLES, D. 1982 Prospects for useful research on coherent structure in turbulent shear flow. In *Surveys in Fluid Mechanics* (ed. R. Narasimha & S. M. Deshpande), pp. 17–33. Bangalore: Indian Academy of Sciences.

DUMAS, R., BONMARIN, P. & FULACHIER, L. 1982 Visualizations of turbulent structures of wakes and boundary layers. In *Structure of Turbulence in Heat and Mass Transfer* (ed. Z. P. Zaric), pp. 551–561. New York: Hemisphere.

FERRE I VIDAL, J. A. 1986 Aplicacio d'algoritmes d'intel-ligencia artificial al reconeixement d'estructures coherents en els fluxos turbulents. Ph.D. thesis, University of Barcelona, Facultad de Quimica, Tarragona.

GRANT, H. L. 1958 Large eddies of turbulent motion. *J. Fluid Mech.* **4**, 149–190.

HAYAKAWA, M. & HUSSAIN, A. K. M. F. 1985 Eduction of coherent structures in the turbulent plane wake. *Proc. Fifth Symp. on Turbulent Shear Flows*, Cornell University, pp. 4.33–4.38.

HUSSAIN, A. K. M. F. 1983 Coherent structures – reality and myth. *Phys. Fluids* **26**, 2816–2850.

KEFFER, J. F. 1965 The uniform distortion of a turbulent wake. *J. Fluid Mech.* **22**, 136–159.

KIYA, M. & MATSUMURA, M. 1985 Turbulence structure in intermediate wake of a circular cylinder. *Bull. JSME* **28**, 2617–2624.

LUMLEY, J. L. 1981 Coherent structures in turbulence. In *Transition and Turbulence* (ed. R. E. Meyer), pp. 215–242. Academic.

MATSUI, T. & OKUDE, M. 1981 Vortex pairing in a Kármán vortex street. *Proc. Seventh Symp. on Turbulence*, University of Missouri-Rolla, pp. 41-1 to 41-7.

MATSUI, T. & OKUDE, M. 1983 Formation of the secondary vortex street in the wake of a circular cylinder. In *Structure of Complex Turbulent Shear Flow* (ed. R. Dumas & L. Fulachier), pp. 156–164. Springer.

MUMFORD, J. C. 1983 The structure of the large eddies in fully developed turbulent shear flows. Part 2. The plane wake. *J. Fluid Mech.* **137**, 447–456.

PAPAILIOU, D. D. & LYKOUDIS, P. S. 1974 Turbulent vortex streets and the entrainment mechanism of the turbulent wake. *J. Fluid Mech.* **62**, 11–31.

PAYNE, F. R. & LUMLEY, J. L. 1967 Large eddy structure of a turbulent wake behind a circular cylinder. *Phys. Fluids Suppl.* S194–S196.

PERRY, A. E., CHONG, M. S. & LIM, T. T. 1982 The vortex-shedding process behind two-dimensional bluff bodies. *J. Fluid Mech.* **116**, 88–90.

ROSHKO, A. 1976 Structure of turbulent shear flows: a new look. *AIAA Paper* 76–78.

SAVILL, A. M. 1983 The turbulence structure of a highly curved two-dimensional wake. In *Structure of Complex Turbulent Shear Flow* (ed. R. Dumas & L. Fulachier), pp. 185–197. Springer.

TANEDA, S. 1959 Downstream development of the wakes behind cylinders. *J. Phys. Soc. Japan* **14**, 843–848.

THOMANN, H. 1959 Measurement of the recovery temperature in the wake of a cylinder and of a wedge at Mach numbers between 0.5 and 3. *FFA Rep.* 84. The Aeronautical Research Institute of Sweden.

TOWNSEND, A. A. 1976 *The Structure of Turbulent Shear Flow*, 2nd edn. Cambridge University Press.

TOWNSEND, A. A. 1979 Flow patterns of large eddies in a wake and in a boundary layer. *J. Fluid Mech.* **95**, 515–537.

WLEZIEN, R. W. 1981 The evolution of the low-wavenumber structure in a turbulent wake. Ph.D. thesis, Illinois Institute of Technology.

WYGNANSKI, I., CHAMPAGNE, F. & MARASLI, B. 1986 On the large-scale structures in two-dimensional small-deficit, turbulent wakes. *J. Fluid Mech.* **168**, 31–71.

ZDRAVKOVICH, M. M. 1969 Smoke observations of the formation of a Kármán vortex street. *J. Fluid Mech.* **37**, 491–496.